Available online at www.sciencedirect.com

jmr&t Journal of Materials Research and Technology

journal homepage: www.elsevier.com/locate/jmrt

Interior defect-induced crack initiation mechanism and initial growth behavior for Ti6Al4V alloy fabricated using laser powder bed fusion

Fulin Liu [a,b,c], *Yao Chen* [a,b], *Lang Li* [a,b], *Chong Wang* [a,b], *Qingyuan Wang* [a,b,**], *Yongjie Liu* [a,b,*]

[a] *Failure Mechanics and Engineering Disaster Prevention Key Laboratory of Sichuan Province, Sichuan University, Chengdu, 610207, China*

[b] *MOE Key Laboratory of Deep Earth Science and Engineering, College of Architecture and Environment, Sichuan University, Chengdu, 610065, China*

[c] *School of Mechanical and Aerospace Engineering, Nanyang Technological University, Singapore, 639798, Republic of Singapore*

ARTICLE INFO

Article history:
Received 27 June 2022
Accepted 11 October 2022
Available online 17 October 2022

Keywords:
Laser powder bed fusion (LPBF)
Ti6Al4V alloy
Very high cycle fatigue (VHCF)
Fine granular area (FGA)
Dislocations

ABSTRACT

The interior defect-induced crack initiation mechanism and early growth behavior of Ti6Al4V alloy fabricated by laser powder bed fusion (LPBF) has been investigated in very high cycle fatigue (VHCF) regime. *P*–*S*–*N* curves under 10% and 90% failure probabilities are obtained in VHCF regime. The cracks inside the early stages of fine granular area (FGA) formation are driven by the maximum shear stress and propagate as Mode II + III mixed cracks. It can be found that the FGA region is composed of many discontinuous nanograins for Ti6Al4V alloys manufactured by LPBF, which are responsible for grain refinement. Grain refinement is associated with dislocation movement within the martensite laths. Dislocation pileup and rearrangement in martensitic laths form dislocation cells, which further develop into nanograins and low angle boundaries. Besides, both the fatigue loading process and the LPBF process form their respective microvoids, which merge and aggregate with each other, thus accelerating the microcrack extension.

1. Introduction

With the integration of aerospace structural components and the demand for lightweight development trends, the traditional preparation method for Ti6Al4V alloy has become difficult to meet the requirements for precision and complex parts. The emergency of additive manufacturing (AM) technology has been developed to solve the problem of manufacturing precision components for Ti6Al4V alloy. The three-dimensional (3D) model data is employed to AM technology through direct information input, making its

* Corresponding author.
** Corresponding author.
E-mail addresses: wangqy@scu.edu.cn (Q. Wang), liuyongjie@scu.edu.cn (Y. Liu).

https://doi.org/10.1016/j.jmrt.2022.10.043

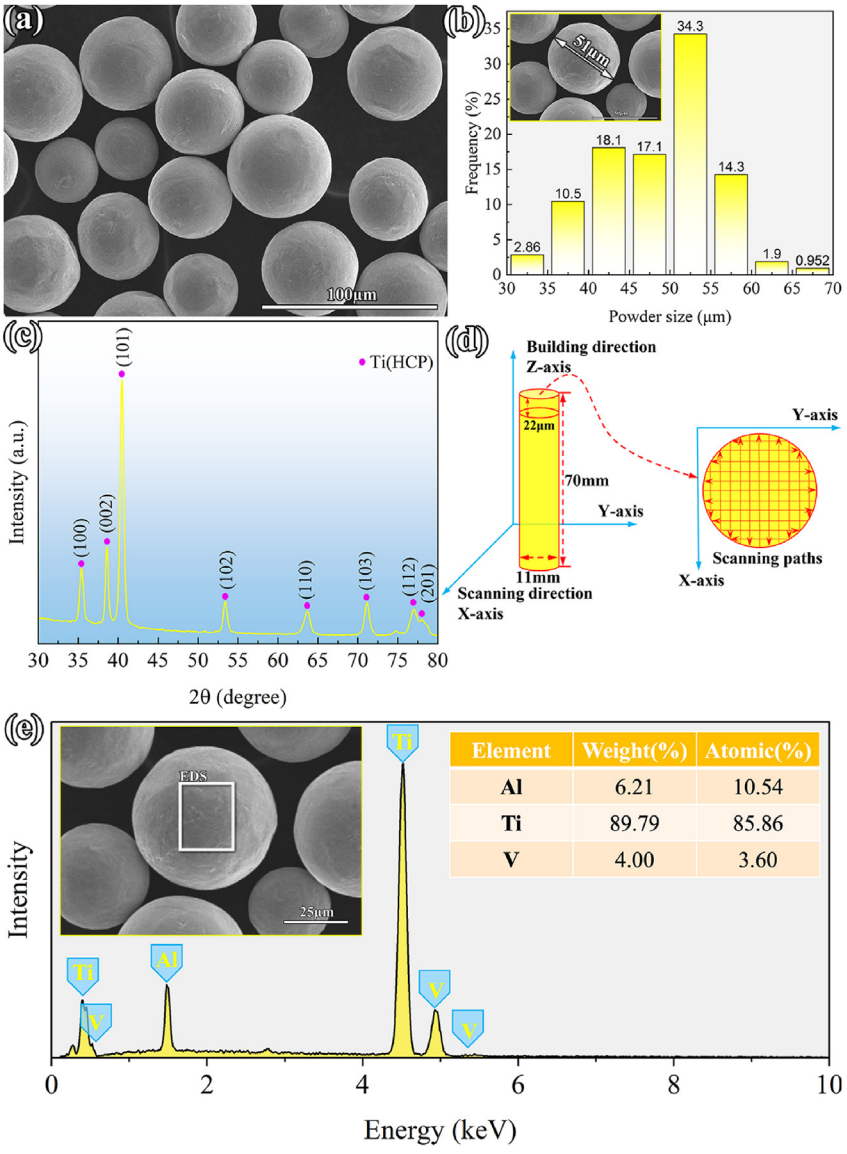

Fig. 1 – (a) The spherical powder of Ti6Al4V alloys; (b) size distribution of the Ti6Al4V alloy powder used for the LPBF process; (c) XRD results of the powder; (d) the printing strategy and scanning paths of LPBF manufacturing Ti6Al4V alloy rod; (e) the chemical composition of the powder based EDS.

development a potential production approach for the aerospace industry [1]. This technology can be expected to provide remarkable opportunities, such as providing intricate geometries, saving expensive metal materials, and shortening lead times [1–3].

As one of the most popular AM technologies, laser powder bed fusion (LPBF) process is based on the principle of rapid prototyping by melting solid powder materials through high-energy lasers, then laying the powder in a layer by layer approach, cooling and solidifying them, and finally superimposed into a 3D part [3]. However, the parameters of the LPBF process, molding microstructures, and unavoidable defects have a considerable impact on the structural integrity of Ti6Al4V titanium alloy. The key structural components manufactured by LPBF for Ti6Al4V alloy in the aerospace industry should be reliable under various complex dynamic loadings in different environments. Compared to conventional subtractive fabrication of Ti6Al4V alloy, the microstructure of LPBF manufacturing Ti6Al4V alloys is finer, resulting in relatively higher static strength [4]. Furthermore, the internal defects inside Ti6Al4V alloys fabricated by LPBF hardly reduce the tensile strength [2,5], so the tensile properties of their parts fabricated from LPBF Ti6Al4V alloys are usually in line with the industrial standards and specifications [1,6]. However, as components of Ti6Al4V alloys fabricated by LPBF process that require a long service time, the presence of defects within the materials severely limits the fatigue performance [1,2,7], thus affecting service life, especially in very high cycle fatigue (VHCF) regime. It is currently possible to optimize the process parameters and implement post-treatment processes to minimize the number of defects and release residual stresses inside LPBF Ti6Al4V alloys, as well as to homogenize the

Table 1 – The process parameters of LPBF manufacturing Ti6Al4V alloys in detail.

Type	Process parameters					
LPBF	Laser power P	Spot diameter	Scan speed v	Layer thickness, t	Line offset, l	Energy density, J
Ti6Al4V	500 W	0.08 mm	1010 mm/s	0.022 mm	0.2 mm	112.5 J/mm^3

microstructure to improve the fatigue performance [8–11]. However, it is still not possible to completely eliminate the defects within the Ti6Al4V titanium alloy fabricated by LPBF process.

The fatigue performance of LPBF Ti6Al4V alloys is particularly sensitive to defects in the very-long life service condition [1,5,10,12]. Although the defects can be closed by the treatment of hot isostatic pressing to improve the service life, it still will lead to cracks developing from the defects [9,10]. J. Günther et al. [10] subjected the LPBF Ti6Al4V alloys to hot isostatic pressing prior to fatigue experiments in the VHCF regime. They found that the fatigue properties of the treated materials were similar to those of conventionally forged materials. This demonstrated that hot isostatic pressing could indeed improve the fatigue properties of LPBF Ti6Al4V alloys. However, considering the large parts and high costs, it makes the popularization of the hot isostatic pressuring method difficult. Therefore, defect-induced fatigue failure has become the focus of research in the LPBF manufacturing Ti6Al4V alloys in the VHCF regime. Liu et al. [5] investigated the VHCF performance of LPBF Ti6Al4V alloys and found that not only did the size and location of the defects control the fatigue life but also the shape of the defects dramatically dominated the fatigue life. The core part of VHCF failure is the fine granular area, whose formation is attributed to the microstructure of the materials and therefore consumes the vast majority of the fatigue life [13,14], as well as forming a rough zone for crack initiation. It makes the existing studies focus on the FGA region, especially on the fatigue failure induced by defects subjected to the VHCF regime for LPBF Ti6Al4V alloys. Du et al. [15] studied the fatigue performance of LPBF Ti6Al4V alloys under two stress ratios up to VHCF regime. They found that only one nanograin layer existed in the crack initiation zone at the stress ratio of R = −1. Sun et al. [9] investigated the fatigue properties of Ti6Al4V alloys fabricated by LPBF after hot isostatic pressing treatment based on ultrasonic accelerated vibration fatigue experiments, and they thought that the grain refinement induced by the interaction of dislocations was responsible for the mechanism of crack initiation and early propagation. However, they did not observe how the dislocations interacted with each other specifically. Therefore, the mechanism of crack initiation and initial propagation based on dislocation motion is further investigated for LPBF Ti6Al4V alloys in VHCF regime.

In this investigation, fatigue experiments were performed on LPBF manufacturing Ti6Al4V alloys up to the VHCF regime using ultrasonic accelerated vibration fatigue testing equipment. The powder of Ti6Al4V alloys was analyzed using X-ray Diffraction (XRD) and scanning electron microscope equipped with an element energy dispersive spectroscopy system (EDS). The microstructure and fatigue fracture surface of LPBF Ti6Al4V alloys were identified by SEM. The inner and outer regions of the FGA were sampled using a focused ion beam (FIB) system and later observed with a transmission electron microscope (TEM). The TEM foils were then characterized by transmission kikuchi diffraction (TKD). The formation mechanism of FGA layer and the mechanism of crack initiation and initial propagation were analyzed and discussed.

2. Materials and methods

2.1. Materials

The LPBF technology was employed to fabricate the Ti6Al4V titanium alloys investigated in the study. The molten pool in the building environment was protected by pure argon gas to prevent air from entering, thereby avoiding damaging the atmosphere. The spherical powder of Ti6Al4V alloys in Fig. 1(a) used for fabricating the samples is ~30–70 μm in diameter. The size distribution of the Ti6Al4V powder is presented in Fig. 1(b). The powder size used for the LPBF process is mainly in the range of 50–55 μm. The XRD results of the Ti6Al4V powder is shown in Fig. 1(c), which can only observe the presence of α phase. The main chemical compositions of Ti6Al4V alloys powder are 6.21% Al, 4.00% V, and balance Ti in wt, respectively, as indicated in Fig. 1(e). The detailed process parameters of LPBF to produce Ti6Al4V alloys were shown in Table 1. Combining all LPBF manufacturing parameters, the input energy density of laser J could be obtained by the following Eq. (1) to be 112.5 J/mm^3.

$$J = \frac{P}{lvt} \tag{1}$$

where P means the laser power; l indicates the line offset; v is scan speed; t shows layer thickness. Moreover, the titanium alloy substrate was heated to 60 °C before LPBF preparation. The building strategy and scanning path of LPBF to produce Ti6Al4V alloys were shown in Fig. 1(d). The final as-built titanium alloy rod manufactured by LPBF with a length along the z-axis of 70 mm and a diameter of 11 mm was obtained.

A metallographic sample was extracted from a titanium alloy rod fabricated by LPBF. The sample surface was gradually mechanically polished to a mirror state using metallographic sandpapers, and then chemically etched with Kroll's reagent (75 mL H_2O + 10 mL HF + 15 mL HNO_3 for 10 s) to expose the microstructure of the sample surface. Finally, the Olympus GX53 optical microscope (OM) was applied to observe the sample surface. Fig. 2(a) represents the microstructure of LPBF Ti6Al4V alloy along the building direction. The prior columnar β grains grow along the building direction and pass through multiple cladding layers, which can be observed in Fig. 2(a). It is worth noting that a large number of fine and lamellar α/α′ martensite laths are distributed inside or outside the β grains, which are attributed to the rapid solidification rate and large thermal gradient in the molten pool

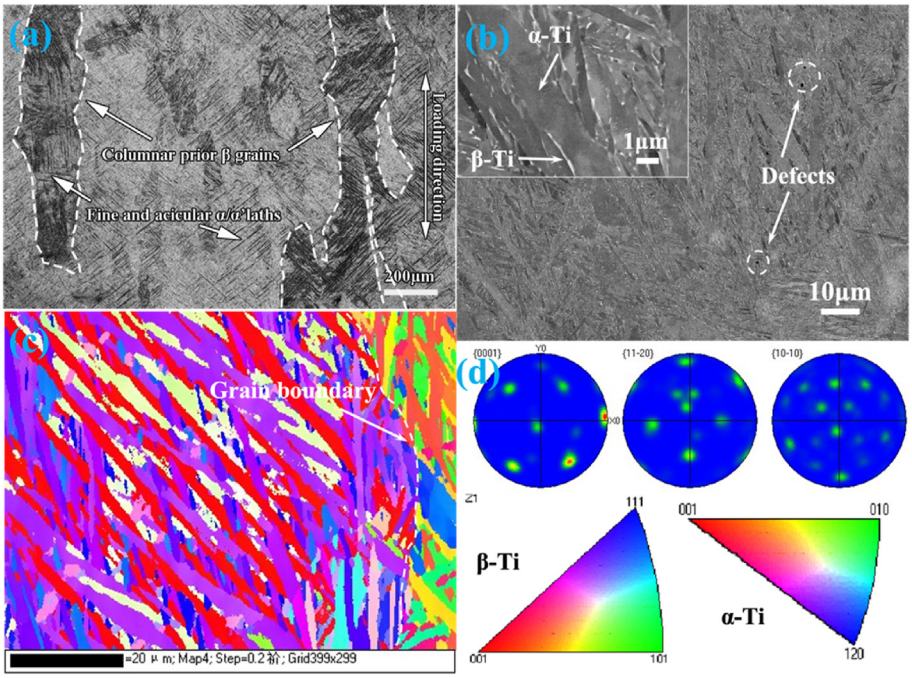

Fig. 2 – (a) The original microstructure of as-built LPBF Ti6Al4V alloy by OM observation; (b) fine acicular microstructure under SEM observation; (c) the inverse pole figure of microstructure; (d) the corresponding pole figure.

[16,17]. The microstructure of the LPBF Ti6Al4V alloy was further analyzed using scanning electron microscopy (SEM), and the results were shown in Fig. 2(b). In the SEM image, it is possible to find many elongated martensitic laths freely distributed in the microstructure. It was noteworthy that defects formed during the LPBF process were found in this image. The results of the high magnification observation were embedded in Fig. 2(b). A small amount of β phase was distributed on both sides of the α martensite laths. This indicated that the LPBF Ti6Al4V alloy was mainly dominated by the α phases with a low content of the β phases. Fig. 2(c) represented the inverse pole figure (IPF) results of electron backscatter diffraction (EBSD) characterization of this microstructure, which revealed the presence of many elongated martensitic laths of similar orientation within one grain. Fig. 2(d) exposed the results of the polar figure (PF) of this characterized part, where it could be found that there was a certain strong (0001) texture obtained from the EBSD scan. The monotonic tensile experiments of LPBF Ti6Al4V alloy have been investigated in the previous study [5]. Its ultimate tensile strength, yield strength, and elongation at failure were approximately 1078 MPa, 886 MPa, and 19.1%, respectively.

2.2. *Ultrasonic fatigue tests*

In order to achieve 10^9 cycles of fatigue loading up to VHCF regime, USF2000, a commercial ultrasonic accelerated vibration fatigue equipment, was employed. All ultrasonic fatigue testers are designed based on the principle of piezoelectric magnetostriction. The fatigue tester transforms electrical signals into high-frequency mechanical waves to excite the specimen, causing the specimen to resonate, thus achieving the purpose of loading. The fatigue system adopted a sinusoidal wave for symmetric tension-compression loading and had a loading frequency of 20 kHz, which could obtain very-long life cycles in a relatively short time. The specimen

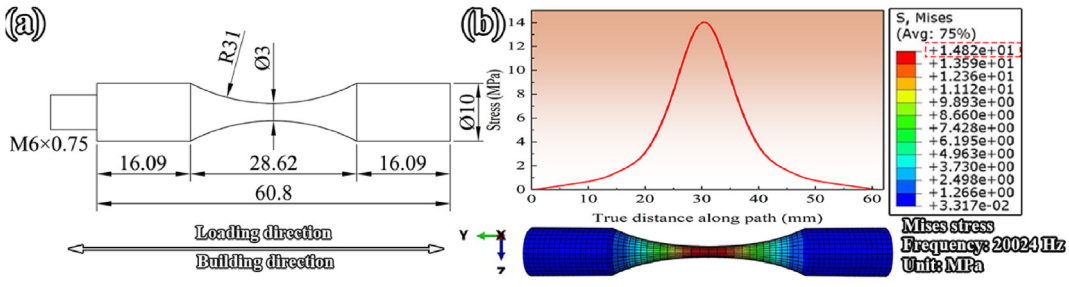

Fig. 3 – (a) The dimensions of ultrasonic fatigue specimen (units: mm); (b) stress distribution of variable section when 1 μm vibration displacement applied to the specimen extremity of Harmonic response analysis.

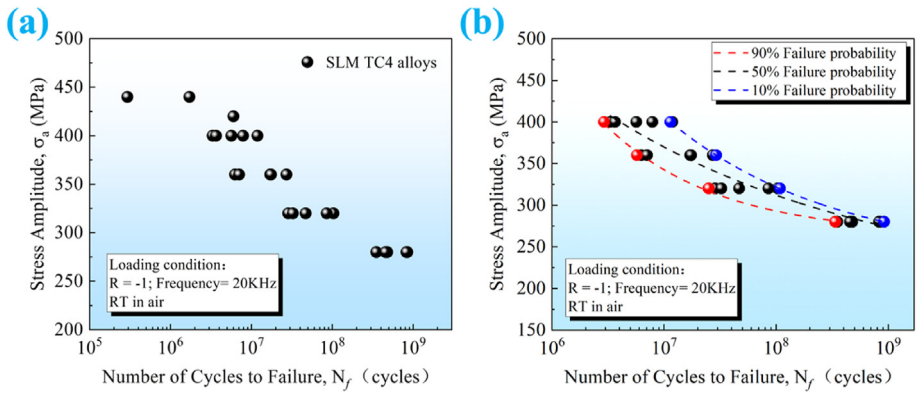

Fig. 4 – S–N results (a) and P–S–N curves (b) of LPBF Ti6Al4V in the VHCF regime.

design for the ultrasonic fatigue tests is different from that of the conventional fatigue tests. In conventional fatigue loading, forced vibration is mostly used, that is, the loading frequency is inconsistent with the natural frequency of specimen size. In terms of the ultrasonic loading, the natural frequency of the specimen itself should be consistent with that of ultrasonic loading, that is, up to 20 kHz. The resonance amplitude is a function of specimen geometry, and the stress amplitude is different in each cross-section [18]. The size of ultrasonic fatigue specimens to meet resonance requirements with a frequency of 20 kHz can be determined by conventional theoretical calculations and finite element methods. Therefore, the specimen size of the ultrasonic fatigue tests was designed by using the finite element methods through the commercial software ABAQUS in the current investigation. The results of specimen sizes were as shown in Fig. 3(a). The minimum section diameter of the designed fatigue specimen is 3 mm, and the total length of the specimen is 60.8 mm. The stress distribution of the designed ultrasonic fatigue specimens was calculated by harmonic response analysis with the software ABAQUS, as presented in Fig. 3(b). The results show that the specimen of these sizes are subjected to tensile and compressive vibrations at a frequency of 20,024 Hz. Hence, the frequency of 20,024 Hz is the intrinsic frequency of the specimen geometry for ultrasonic fatigue loading. It is worth noting that when a vibration displacement of 1 μm is applied to the specimen extremity, the maximum stress value in the middle minimum section of the specimen is 14.82 MPa in Fig. 3(b). The ratio of the maximum stress value for the middle minimum section to the displacement of the specimen extremity is called the displacement-stress coefficient, in MPa/μm. So, the calculated displacement-stress coefficient of the specimen size is 14.82 MPa/μm. In other words, when the extremity of the fatigue specimen is subjected to a vibration displacement of 1 μm, the middle minimum section will be applied with a maximum stress amplitude of 14.82 MPa. The design of test specimen size and the principles of the ultrasonic fatigue test system were described in detail by Bathias in his book "Gigacycle Fatigue in Mechanical Practice" [19]. During the fatigue tests, the vibration displacement of the specimen extremity was adjusted to control the target stress amplitude required during the fatigue period of the specimen. For example, to obtain the target stress of 400 MPa, a displacement of 400/14.82 = 26.99 μm should be input on the specimen extremity. In addition, compressed cold air was used to cool the high temperature of specimens attributed to ultra-high frequency loading to maintain the temperature within the range of room temperature during the test process. It is worth mentioning that the loading direction for the fatigue specimen is consistent with the building direction.

2.3. *Observation and characterization*

The fracture morphology after fatigue failure was observed by using a SEM-EDS (JEOL6510LV and EDAX) to determine fracture features and crack initiation modes. To further investigate the crack initiation and early propagation mechanism of FGA, a three-dimension (3D) dual-beam system consisting of a focused ion beam (FIB) and a SEM (SEM-FIB, JIB4700F) was employed to conduct fixed-point sampling at the crack initiation zone. One TEM thin foil sample was extracted inside the FGA region and close to the defect, and the other was outside the FGA and in the stable crack growth region. The TEM foils were extracted along the loading direction, that is, the building direction. During FIB milling, the fracture surface of the extracted sample was protected by a platinum (Pt) layer. When the FIB milling was complete, the transmission electron microscope (TEM, JEM-F200) was applied to observe the TEM thin foils extracted by FIB milling to reveal the dislocation distribution. Moreover, the crystallographic orientation of TEM foils was further analyzed by using the Transmission Kikuchi Diffraction (TKD) technique at high resolution. The Channel 5 software was employed to analyze the TKD results. The distribution of plastic deformation of microstructure after fatigue was determined by the Kernel average misorientation (KAM) mapping.

3. Results and discussion

3.1. *Fatigue lifetime*

Fig. 4(a) presents the S–N (i.e. stress amplitude – fatigue lifetime) results of LPBF Ti6Al4V alloys in the VHCF regime at room temperature. The S–N results show that the fatigue life can increase as the applied stress amplitude decrease and that

Table 2 – The mean and standard deviation of logarithmic fatigue life ($logN_f$) at different stress amplitudes for LPBF Ti6Al4V alloys.

Stress amplitude (MPa)	280	320	360	400
Mean, μ	8.7460	7.7169	7.1115	6.7617
Standard deviation, S	0.1694	0.2481	0.2755	0.2311
Number of fatigue data, n	5	5	5	5

there is no conventional fatigue limit for LPBF Ti6l4V alloys. The fatigue lifetime of LPBF Ti6Al4V alloys varies from 10^5 to 10^9 cycles, while the corresponding stress amplitude varies from 440 MPa to 280 MPa in Fig. 4(a). At 10^9 cycles, the fatigue strength of LPBF Ti6Al4V alloys is closed to 280 MPa, which can be regarded as the fatigue limit for LPBF Ti6Al4V alloys in the VHCF regime.

The classic three-parameter formula (i.e. $(\sigma_a - \sigma_w)^a \times N_f = b$) was employed to assess the S–N curve of LPBF Ti6Al4V alloys, where σ_a was the stress amplitude; N_f showed the fatigue life; σ_w, a and b were some material-dependent constants [20]. Using the least-squares method to fit the fatigue data with this formula, the specific values of σ_w, a and b can be determined, so that the relationship between the stress amplitude and the fatigue life can be obtained, that is, $(\sigma_a - 198.5)^{5.584} \times N_f = 2.988E19$.

Considering the material inhomogeneity, processing deviation, environment and other factors affecting the fatigue test results, this makes the fatigue test data have a large dispersion. The S–N curve fitted by the three-parameter formula had only a 50% high failure probability in Fig. 4(b) and is not therefore unsuitable for further applications of LPBF Ti6Al4V alloys in aerospace and other related fields. In the design and assessment of metallic components, in addition to stress amplitude and fatigue life, the probability of failure is also an important parameter to ensure safety and reliability in service, and therefore the probability of failure should also be taken into account [21]. It is generally known that the fatigue probabilistic S–N (P–S–N) curves under different failure probabilities are more applicable for the fatigue strength design. For fatigue strength design, it is more applicable to obtain the P–S–N curves of materials under different failure probabilities. The P–S–N curves effectively solve the uncertainty introduced by the dispersion of fatigue life of materials, so that they can be used as a more intuitive basis for strength design. In addition, the P–S–N curves can express the relationship between stress amplitude and fatigue life at different failure levels to determine the degree of life dispersion of the material at different stresses.

Before describing the P–S–N curve, the distribution of logarithmic fatigue life ($log\ N_f$) for LPBF Ti6Al4V alloys under each stress amplitude condition is examined using the cumulative probability function form of the normal distribution, which is as follow:

$$P(N < N_f) = \int_{-\infty}^{\log N_f} f(N)dN = \frac{1}{2}\left\{1 + erf\left[(\log N_f - \mu) \Big/ \sqrt{2S^2}\right]\right\} \quad (2)$$

where $erf(x)$ means the Gauss error function, μ is the mean value of $log\ N_f$, S depicts the standard deviation. First, consider the number of fatigue data points under each stress amplitude as n, where the number of fatigue data points under each stress amplitude is 5, that is, $n = 5$. Then, the 5 fatigue data points under each stress amplitude are sorted from low to high in the order, and the sorting number is i ($i = 1, 2, 3, 4, 5$). Next, divide the sorting number by (n+1), (i.e. $i/(n+1)$). The relevant data parameters for the $log\ N_f$ probability distribution examination are given in Table 2. Thus, the cumulative probability curves of $log\ N_f$ for each stress amplitude are presented in Fig. 5, which indicate that the $log\ N_f$ results under each stress condition followed the normal distribution. Based on these, the fatigue life distribution curves of LPBF Ti6Al4V alloys under different failure probabilities in the VHCF regime could be obtained using the three-parameter formula:

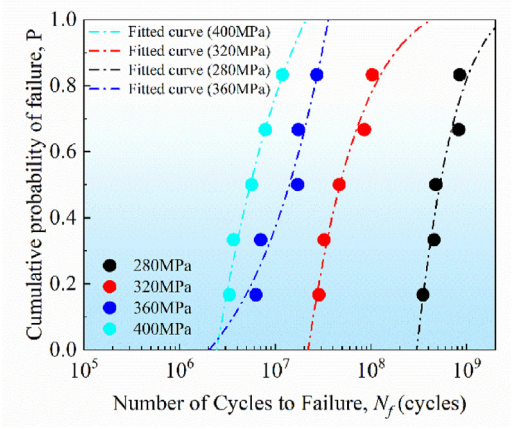

Fig. 5 – The normal distribution of fatigue life at different stress amplitudes.

(1) 10% failure probability: $(\sigma_a - 234.4)^{3.403} \times N_f = 4.061E14$
(2) 90% failure probability: $(\sigma_a - 263.7)^{2.316} \times N_f = 2.474E11$

Therefore, the failure probability of P–S–N curves at 10% and 90% in the VHCF regime are also represented in Fig. 4(b), and the results show that the P–S–N curves are a good way to assess the fatigue life distribution of LPBF Ti6Al4V alloys at each stress amplitude in the VHCF regime.

3.2. SEM observation of fracture surface

Fig. 6 presents a typical internal fracture with similar characteristics to the internal fracture of high-strength steels induced by inclusions in the VHCF regime, except that the cracks are initiated by defects within materials. Different from traditional wrought titanium alloys, where cracks mainly originate in the weak primary α phases [22,23] and sites with heterogeneous phase distribution inside materials [24], the cracks in LPBF Ti6Al4V alloys are almost always initiated from internal defects, either regular defects formed by escaping gas or the irregular defects produced by lack of fusion. In Fig. 6(a), it can be found that the fatigue fracture of internal crack initiation is divided into 4 zones, namely the outermost instantaneous fracture zone, followed by the rapid crack propagation zone and the stable crack propagation zone, as well as the most central crack initiation zone. In the crack

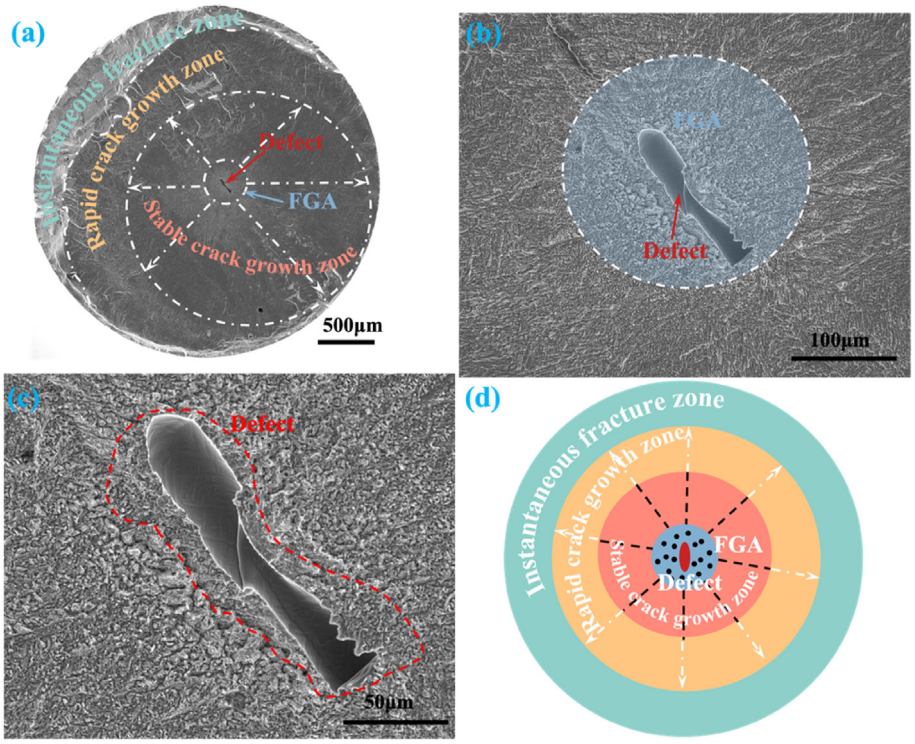

Fig. 6 – Internal fatal defect induced fatigue failure: (a) Overall fracture surface; (b) FGA with the defect in the crack initiation zone; (c) uneven morphology around the defect; (b) schematic diagram of defect induced crack initiation and propagation (σ_a = 280 MPa, N_f = 3.510 × 10^8).

initiation zone, an irregular elongated defect is found. It can be explained that the defect induced crack initiation and early propagation during the fatigue process. A circle of the fine granular area around the fatal defect is called the FGA in Fig. 6(b). Further observation reveals that the particle size inside the red dashed line around the defect is smaller than that outside the red dashed line, and the particle size outside the dashed line gradually decreases with the distance away from

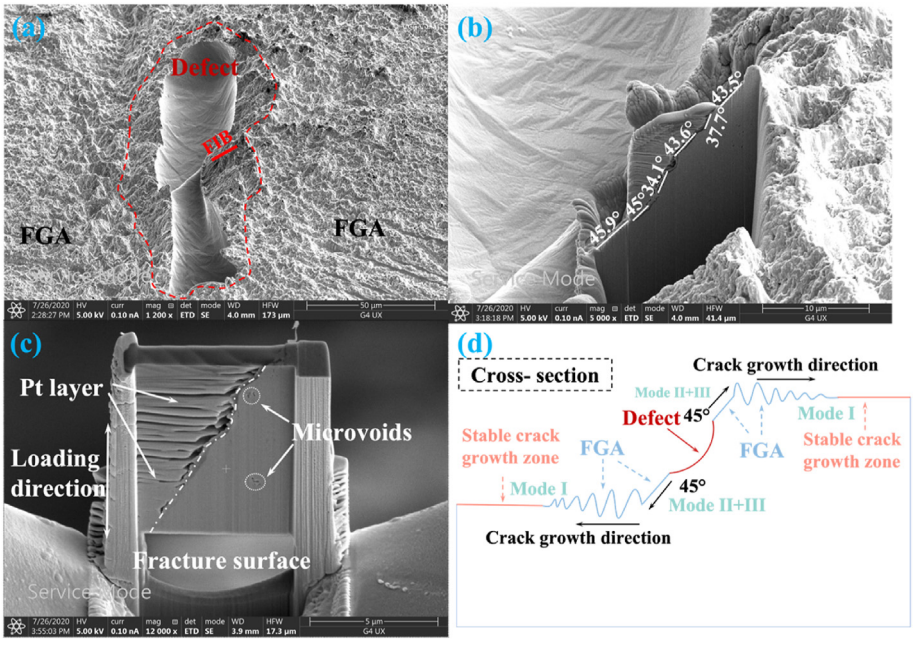

Fig. 7 – (a) Morphology of crack initiation zone and crack surface location exposed by FIB in (b) and (c); (d) schematical illustration of the crack early propagation in the FGA (σ_a = 280 MPa, N_f = 3.510 × 10^8).

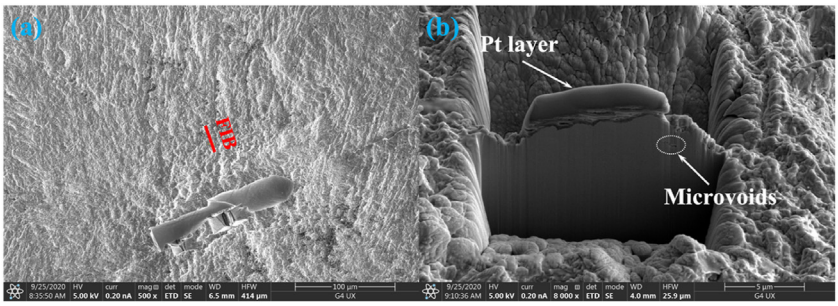

Fig. 8 – (a) Crack surface location outside the FGA exposed by FIB in (b) (σ_a = 280 MPa, N_f = 3.510 × 10^8).

the defect in Fig. 6(c). Fig. 6(d) shows a schematic diagram of the fracture surface of the defect-induced internal crack initiation and propagation in VHCF regime for LPBF Ti6Al4V alloys.

The formation of four distinct crack propagation zones in the fracture surface is related to the stress intensity factor (K) at the crack tip. When the stress intensity factor (K) is less than the steady-state propagation threshold (K_{th}) for defects-induced internal crack ($K < K_{th}$), the microcracks that initiate from the fatal defect are affected by the martensitic laths inside the LPBF Ti6Al4V alloys, and the microcracks development fragments the martensitic laths, resulting in the formation of FGA [5]. This microcrack propagation process in the FGA region consumes almost all of the fatigue life [25]. When the stress intensity factor (K) at the crack tip reaches the threshold value (K_{th}) ($K = K_{th}$), the crack transforms from short crack propagation to long crack propagation. Then, the main crack propagates at a steady rate, which is in accordance with the Paris law, and thus a stable crack propagation zone is formed outside the FGA as the center when the stress factor intensity factor (K) at the crack tip is more than the threshold value (K_{th}) (i.e. $K > K_{th}$). As the crack length increases, the stress intensity factor (K) at the crack tip further increases, the crack propagation rate also increases, and the crack propagation enters the rapid crack propagation zone. Eventually, the instantaneous fracture can occur.

3.3. *Early crack propagation behavior*

The morphology of the crack initiation zone adjacent to the fatal defect was performed using a 3D dual-beam SEM-FIB, and the results were shown in Fig. 7. The fatal defect presents an inclined trend in the crack initiation area, that is, the whole FGA is not the plane shown in Fig. 6(b). There are much finer roughness around the fatal defect in the tilted surface (inside the red dotted line). The particle features outside the red dotted line have a higher roughness, and gradually decrease in roughness as they get further away from the defect. For the patterns with finer roughness around the defect, it might be attributed to the ultra-low crack expansion rate depending on the sensitivity to microstructure under the fatigue loading process. After FIB milling in Fig. 7(b), the short crack propagation profiles on the fatal defect side could be well exposed to elucidate the crack driving forces. The orientations of short crack propagation close to the defect side in Fig. 7(b) are 45.9° and 45° concerning the loading direction. It can be speculated that the short crack propagation inside the FGA region along the directions (45.9° and 45°) is close to the direction of maximum shear stress. Then, the crack propagation path is deflected to 34.1°. Next, the short crack propagation orientation is extended at 43.6° → 37.7° → 43.5° with respect to the tensile axis. This illustrates the branching phenomenon of short cracks in the initial extension in the crack initiation zone. Unfavorable grain orientation may impede crack propagation in one direction, thus resulting in a relatively large angular deflection. Fig. 7(c) shows the entire TEM foil, and it can be found that the orientation of the entire fracture surface is evaluated as about 40°, which is very close to the maximum shear stress direction. This implies that when the fatigue life of LPBF Ti6Al4V alloys is up to VHCF regime, the initial propagation of short cracks in the crack initiation zone is driven by the maximum shear stress. In other words, the maximum shear stress provides the driving force for the early formation of FGA in the VHCF regime. From the fracture mechanics point of view, the short cracks in the early stages of FGA formation are Mode II and III owing to the fact that the orientation of the initial crack extension direction is not strictly parallel to the direction of maximum shear stress (45°) [26]. Moreover, in the TEM foil from Fig. 7(c), several microvoids can be found to exist, but it is impossible to determine whether these originate from defects produced by the LPBF process or formed during the fatigue process. Considering the "number cyclic pressing" (NCP) model proposed by Hong et al. [27], the formation of microvoids in the FGA is evident. The initial crack surface is reciprocally pressed to break the martensitic laths in the microstructure, which leads to the formation of microvoids in the crack weakness zone. The formation of such microvoids is attributed only to the fatigue loading process. Regarding the LPBF process, they may be derived from the lack of local laser energy. However, microvoids are able to promote crack expansion during fatigue loading. Fig. 7(d) shows the schematic diagram of the initial extension of short cracks within the FGA region for LPBF Ti6Al4Vs alloy in the VHCF regime. Under the action of cyclic loading, stress concentration occurs in the defects. Short cracks are formed that propagate as Mode II + III cracks and are driven by the maximum shear stress. And then, due to the resistance of microstructure and very low crack extension rate, the grains around the defects are gradually refined while forming inclined planes around the defects.

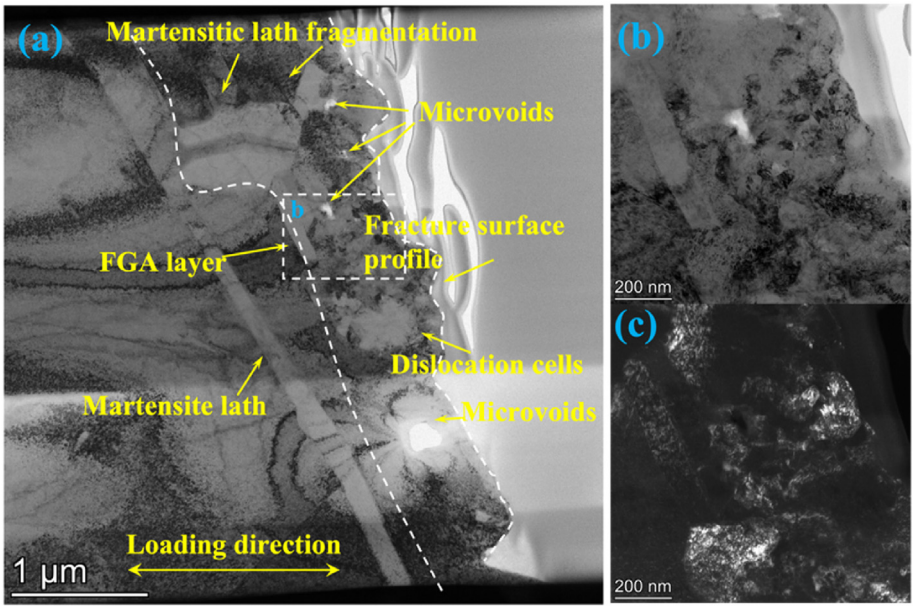

Fig. 9 – TEM observations of the extracted FIB sample near the fatal defect: (a) the fatigued microstructure morphology underneath the fracture surface profile of the FGA region; (b) Dislocation cells and martensitic lath fragmentation; (c) corresponding DF image of (b) ($\sigma_a = 280$ MPa, $N_f = 3.510 \times 10^8$).

Fig. 8 shows the FIB milling in the direction of crack growth outside the FGA region to expose the crack growth profile. It can be found that the crack growth profile is basically perpendicular to the loading direction. This indicates that the crack growth in this region is driven by tensile normal stress and extends as Mode I cracks. Besides, on the side close to the FGA region, the presence of microvoids can also be found. In general, the growth driving force of the crack inside the FGA is inconsistent with that of the crack outside the FGA, and the crack growth model is also inconsistent, as shown in Fig. 7(d).

3.4. *Dislocations induced FGA formation*

FGA is commonly found in various metallic structural materials, such as titanium alloys [20,28], high strength steels [27,29,30], aluminum alloys [31], etc. The life required for FGA formation is over 95% of the total fatigue life [13,32], making it the most central feature in VHCF regime. Therefore, most investigations of VHCF have focused on FGA to point of revealing its formation mechanism depending on the sensitivity to microstructure.

In the current investigation, a foil was precisely extracted in the interior of the FGA region near the fatal defect from the failed sample in Fig. 7 up to VHCF regime for TEM observation using the FIB technique along the loading direction and the examination result was presented in Fig. 9. Fig. 9(a) represents the TEM bright-field (BF) image of the fatigued microstructure morphology underneath the fracture surface profile of the FGA region. From this figure, it can be clearly seen that there are dislocation cells with lower dislocation density heterogeneously distributed below the fracture surface profile, constituting an FGA layer with a thickness of about 500–1000 nm. The martensitic lath fragmentation of the fatigued microstructure can also be seen in Fig. 9(a). Subsequent observations in Fig. 10 also confirm this result. In addition, some nano-scale microvoids can be observed in the FGA layer and close to the fracture surface in Fig. 9(a). And the existence of these microvoids may originate from localized damage during the crack initiation and early propagation process. Moreover, the formation of microvoids in the FGA layer for titanium alloy Ti6Al4V in VHCF regime has already been confirmed by other references [24,33]. The size differences of microvoids illustrate different stages of damage development under cyclic loading. Internal nano-scale microvoids located in the FGA region during VHCF regime are considered to be a precursor to the start of interior crack initiation. Certainly, microvoids coalescence leading to crack initiation has been demonstrated in some studies [24,33]. It is noteworthy that a martensite lath penetrates the entire TEM foil, which indicates the original lamellar microstructure in Fig. 2. A high magnification observation of the local area in the FGA layer in Fig. 9(a) is presented in Fig. 9(b) and (c), where Fig. 9(c) is the dark-field (DF) image. In Fig. 9(b), the dislocation cells with lower dislocation density and the result of the martensitic lath fragmentation can be further found. This further demonstrates that the dislocation cells are not homogeneously distributed in the FGA layer. The dislocation cell structures were also observed in the FGA layer of stainless steel subjected to VHCF by Zhu et al. [34]. Fig. 9(c) presents the nanograins with different sizes. This seems to imply that the FGA layer is composed of many discontinuous nanograins. The fatigued microstructure below the fracture surface profile in the FGA region is refined under the cyclic loading process in VHCF regime, thus resulting in nanograins in the LPBF Ti6Al4V alloy. So microstructural evolution plays an instrumental role in the cyclic deformation process subjected to VHCF regime.

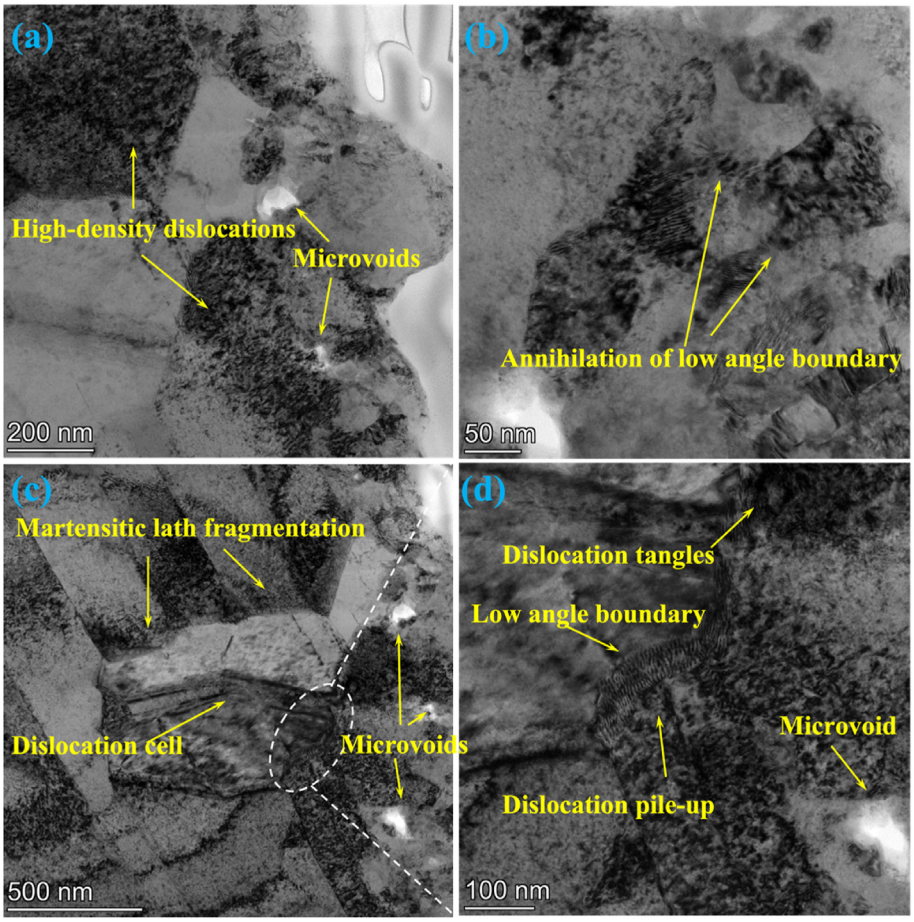

Fig. 10 – High magnification TEM images to observe the FGA layer: (a) the fragmented martensitic lath with high-density dislocations and dislocation cells; (b) annihilation of low angle boundary; (c) and (d) high-density dislocations and low angle boundaries of nanograins (σ_a = 280 MPa, N_f = 3.510 × 10^8).

During cyclic deformation, microstructural evolution is highly associated with dislocation interactions and rearrangement [9,34,35]. Moreover, M. Koster et al. [36] indicated the dislocation cell structure in the FGA region could allow the formation of small subgrains or low-angle grain boundaries of medium carbon steel in VHCF regime, which promoted the formation of discontinuous nanograins layer. In order to further determine the role of dislocation evolution in the formation of FGA for the LPBF Ti6Al4V alloys, the nanograin layer was observed by TEM at high magnification, as presented in Fig. 10. A large number of inhomogeneous and high-density dislocations are prevalent in the fragmented martensitic laths and the dislocations pile up towards the grain boundaries. This indicates a significant strain localization in the deformation behavior of the martensitic laths. Moreover, the dislocation cells can also be found in Fig. 10(a). The annihilation of low angle grain boundary makes the dislocation density between the two nanograins decrease in Fig. 10(a). Fig. 10(b) further verifies the presence of annihilation of low-angle grain boundary as well as martensite pattern with high dislocations. Fig. 10(c) depicts the results presented by rotating the TEM sample in Fig. 10(a) at a certain angle. The presence of the nanograin with low angle boundary and high-density dislocations inside the martensitic laths around the grain boundaries is still observed in Fig. 10(c). The dislocation cell structure is surrounded by a low-angle boundary to further develop the nanograins. Fig. 10(d) also reveals the presence of dislocation entanglement and the formation of low angle boundaries for nanograins in the FGA layer, which is responsible for dislocation rearrangement and interaction. This implies that the formation of the FGA layer is associated with dense dislocation distribution and low angle boundaries formed by dislocation rearrangement. There are indeed dense deformation dislocations inside the fragmented martensitic laths in Fig. 10(d). The dense dislocations are found to rearrange to form low angle boundaries. The formation of low angle boundaries can prove that the current nanograins in the FGA layer are in fact subgrains.

The distribution of dense dislocations in the FGA layer suggests a severe plastic deformation of the microstructure in this region. During the fatigue loading process, significant local stress concentrations occur in the vicinity of the fatal defect within the LPBF Ti6Al4V alloys, resulting in strain incompatibility or stress gradient in the microstructure. The accumulation of the number of cycles makes the strain localization effect increase and the activity of dislocations intensifies. The dislocations become entangled and rearranged, thus forming dislocation cell and low angle

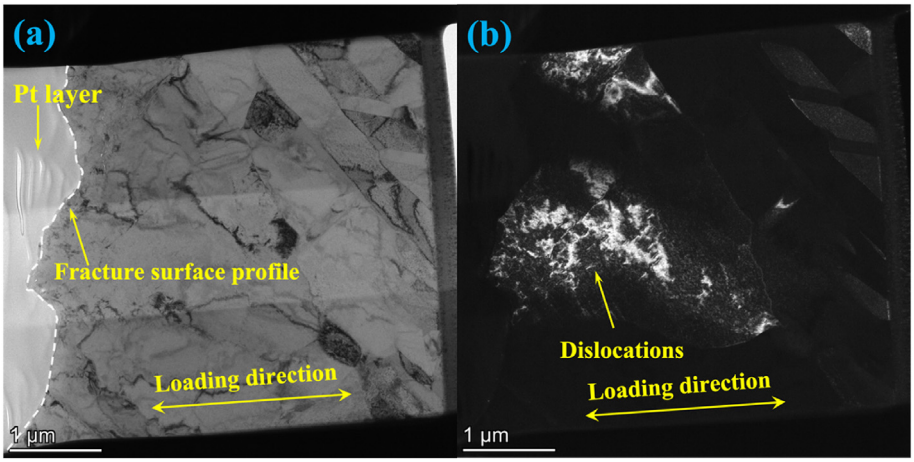

Fig. 11 – TEM observations of the extracted FIB sample outside the FGA region in Fig. 8: (a) BF image; (b) Corresponding to DF image (σ_a = 280 MPa, N_f = 3.510 × 10^8).

boundaries, then the grains possessing low angle boundaries partially develop into subgrains in the nanoscale (i.e. nanograins) alone. Moreover, in Fig. 10, it is also observed that nano-scale microvoids are unevenly distributed in the FGA layer.

TEM sampling of the stable crack propagation zone outside of the FGA region was performed using the FIB and then observed, and the current microstructure examination results for the entire sampling area were shown in Fig. 11. No presence of nanograins was detected in the microstructure characterization after fatigue below the fracture surface profile in Fig. 11(a). Very low dislocation density is also present below the fracture surface profile. The corresponding DF mapping in Fig. 11(b) also reveals that no nanograins are present at this location. However, dislocation rearrangement can still be observed in one of the martensitic lath below the fracture surface profile. This represents the passage of the main crack, which has allowed a certain degree of plastic deformation of the surrounding microstructure. The stress intensity factor range of the FGA region edge (K_{FGA}) is considered to be the threshold value for stable crack expansion (K_{th}) [5]. When the crack propagated beyond the FGA region, the stress intensity factor range at the crack tip is greater than the threshold value (K_{th}), and the crack propagation rate is higher. The crack passes through the microstructure rapidly, and the sensitivity to microstructure is weaker. It is not limited by the microstructure, and it is difficult to form nanograins regions. In contrast, for the interior of the FGA region, the stress intensity factor range of the crack tip is lower than K_{th}, the crack extension is limited by the microstructure. The sensitivity to microstructure is higher, and the crack extends at ultra-low speed in the microstructure, thus promoting nanograins formation.

3.5. *TKD analysis of the extracted samples*

Fig. 12 represents the TKD characterization results with scanning step size of 10 nm of the TEM foil by FIB milling in Fig. 7 inside the FGA region. Fine grains in the nanoscale can be found below the fracture surface profile. This verifies that the FGA layer is indeed composed of many discontinuous nanograins. In addition, the microstructure examination also shows a whole grain characteristic, that is, the bottom part of FGA layer has the same grain orientation and no grain boundaries are observed. This means that under the action of cyclic loading, the grains near the fatal defect are refined, and the re-formed subgrain structure has a different grain orientation. The kernel average misorientation (KAM) was employed to evaluate the local strain gradient distribution of the currently fatigued microstructure [37], as shown in Fig. 12(b). It can be found that the KAM peak values of FGA layer are much higher than that of the intact grains below it, which implies the presence of severe plastic deformation in the nanograin layer and also indicates a higher dislocation density. The TKD results also support the results that are observed by TEM observation. Further careful observation reveals that the KAM peak values near the grain boundary in the newly formed nanograin are higher than the KAM peak values inside the nanograin. This result demonstrates that low angle boundaries formed by the dislocation rearrangement in nanograins do exist. And then in the grain boundary diagram in Fig. 12(c), a large number of low angle boundaries are present in the FGA layer, and the increase in the number of low angle boundaries also reflects the increase in strain localization, i.e., the increase in dislocation density, which can promote crack propagation [38]. More importantly, this substantiates that the low angle boundaries are formed by dislocation rearrangement, which is consistent with the results observed by M. Koster et al. [36] for medium carbon steels subjected to the VHCF regime. Therefore, it can be speculated that the formation of low angle boundaries does not depend on the type of material, but only on the conditions of applied loading.

In order to better understand the distribution of nanograins size inside the FGA layer, we extracted the FGA layer using the software Channel 5, and the corresponding results were shown in Fig. 13. It can be observed that almost all of the nanograin exhibit equiaxed features in the morphology in

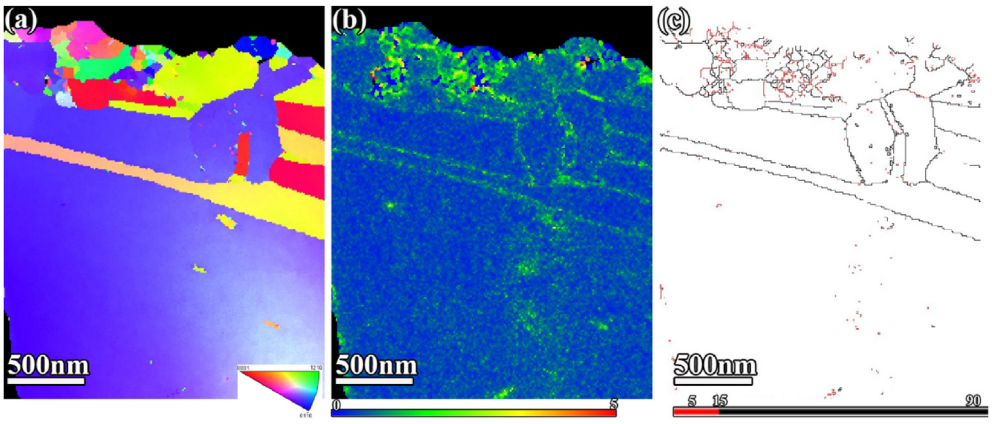

Fig. 12 – TKD results inside the FGA region based on TEM observation in Fig. 9; (a) IPF mapping of fatigued microstructure below fracture surface profile; (b) KAM mapping of the current position; (c) grain boundary of IPF mapping (σ_a = 280 MPa, $N_f = 3.510 \times 10^8$).

Fig. 13(a) while differing from the initial microstructure with fine and acicular features in Fig. 2. Under cyclic loading, the grain morphology in the FGA layer is transformed. All the nanograin sizes are distributed within 800 nm, 46% of them have the diameter in the size range of 100 nm, as depicted by the strong peak in Fig. 13(b). The proportion of nanograin sizes larger than 300 nm is small, and they may not be the final form of martensitic lath fragmentation. It is worth noting that the grain size may increase further away from the fracture surface, where the microstructural is less affected by cyclic loading. Although the size of nanograin has been widely reported, such as Hong et al. [27] (50 nm in high-strength steel), 70 nm reported by Grad et al. [30]. These dimensions of nanograin appear to be consistent with those in our LPBF Ti6Al4V alloy subjected to VHCF regime, that is, all within 100 nm. In summary, the grain morphology and size distribution in the FGA region of the LPBF Ti6Al4V alloy were significantly altered, which was attributed to the action of large amounts of cyclic reciprocal loading.

Fig. 14(a) represents the phase diagram of the FGA layer with nanograin. The content of β phases is rarely and sporadically distributed in the FGA region, and most of the FGA layer is α phases. Fig. 14(b) demonstrates the pole figures of seven selected α grains and three β grains. The purpose here is only to verify the Burgers orientation relationship (BOR) between the β grains and selected α grains after martensitic lath fragmentation. From Fig. 14(c), it can be found that the nano-sized α grains formed after undergoing grain refinement in the FGA layer and the three β grains strictly satisfy the relationship between the slip planes (0001)α//{110}β in the BOR, but not the relationship between the slip directions <11−20>α//<111>β. In other words, the newly formed α nanograins after cyclic deformation still maintain a strict BOR relationship with its β phase. This seems to be the first time that the recrystallized α and β phases have been confirmed in the nanograin layer of FGA still obeying the BOR relationship in VHCF regime.

Fig. 15 expresses the TKD characterization results of the TEM sample by FIB milling of the outside FGA region. In contrast to Fig. 12, the presence of nanograins is not found below in the fracture surface profile, which is also consistent with the TEM observation in Fig. 11. However, the presence of three nanograin-like shapes of different sizes but with the same orientation is found away from the fracture surface profile, as shown in Fig. 15(a). Nevertheless, these grains are found to be β phases by the phase diagram in Fig. 15(c), which is consistent with the distribution of β phases observed in Fig. 2(b), that is, β phases are sporadically distributed at the boundary of α phases. In the KAM diagram of Fig. 15(b), there is no area of high KAM values below the fracture surface

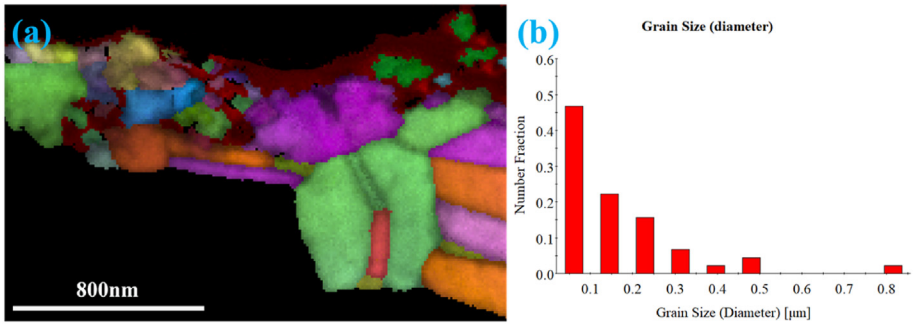

Fig. 13 – Nanograin size measurement: (a) FGA layer with nanograins; (b) statistical distribution of diameter of nanograins (σ_a = 280 MPa, $N_f = 3.510 \times 10^8$).

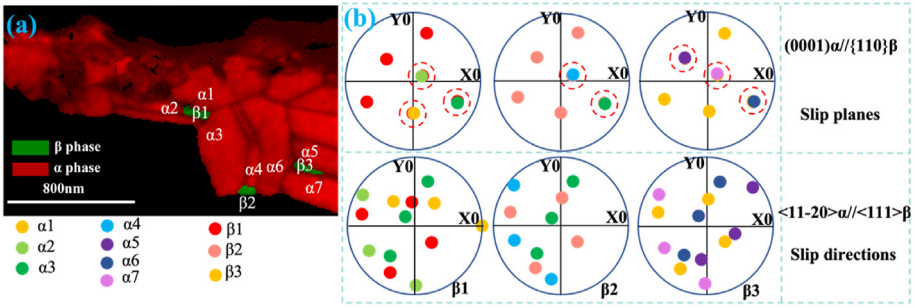

Fig. 14 – (a) Phase mapping of FGA layer; (b) the corresponding pole figures of selected α phase and β phases in the FGA layer, showing that the refinement of the formed α phases obey the Burgers orientation relationship with β phases (σ_a = 280 MPa, $N_f = 3.510 \times 10^8$).

contour, which differs from that in Fig. 12(b). The nanograins formation in the crack initiation zone expends a large amount of lifetime, while the lifetime consumes in the crack propagation zone is almost negligible, lacking the role of NPC, so it is also difficult to form nanograins on the fracture surface. Moreover, compared to other regions of the α phases as reflected in Fig. 15(b), the presence of higher KAM peak values in the three β phase locations are found, which indicates the presence of high strain gradients, i.e., high dislocation density in the β phases. This describes the fact that the β phases are more prone to plastic deformation under the same magnitude of external loading. It is generally known that the β phase in α+β titanium alloys is softer compared to the α phase [39,40]. The results in Fig. 15(b) confirm that this is also present in the LPBF Ti6Al4V alloys. In addition, it is noteworthy that the β phases are all located at the sharp corners of the α-phase grain boundaries. Under the action of external loadings, the sharp corner locations are more pronounced to stress or strain concentrations, which induce higher plastic deformation and dislocation density.

3.6. *Mechanism of crack initiation and early propagation*

Grad et al. [30] reported the formation mechanism of FGA for high-strength steels in VHCF regime. They confirmed by means of FIB-TEM that FGA is constituted by fine grains and observed the dislocation arrangement in the high-strength steel, followed by the transformation into dislocation cells and then the formation of subgrains and low-angle grain boundaries as they proposed the mechanism of localized grain refinement at the crack tip. Chai [41] also concluded that the fine-grain layer was derived from localized cyclic plastic deformation around the defects or inclusions for martensitic steel subjected to the VHCF regime. Sun et al. [9] also identified grain refinement as a result of interactions between dislocations that are dependent on high strain localization of microstructural inhomogeneities. Under tensile-compressive loading (R = −1), D. Spriestersbach [42] suggested that local plastic deformation around inclusions leads to continuous dislocation motion during VHCF loading for high strength steel, where favorable dislocation arrangements will form and remain randomly, after which dislocations develop into an energetically favorable state in the form of dislocation cells. With the continuous growth of lifetime, some dislocation cells with high-density dislocations will stimulate the formation of new grain boundaries to minimize the local elastic energy [42]. For discontinuous fine-grain layers, many investigations [9,27,41,43] have confirmed that the microscopic nature of the FGA region is a thin nanograin layer [27] and that the formation process of the FGA region is a continuous grain refinement process [30]. A considerable number of models have been proposed for the origin of nanograins, such as the NPC model proposed by Hong et al. [27].

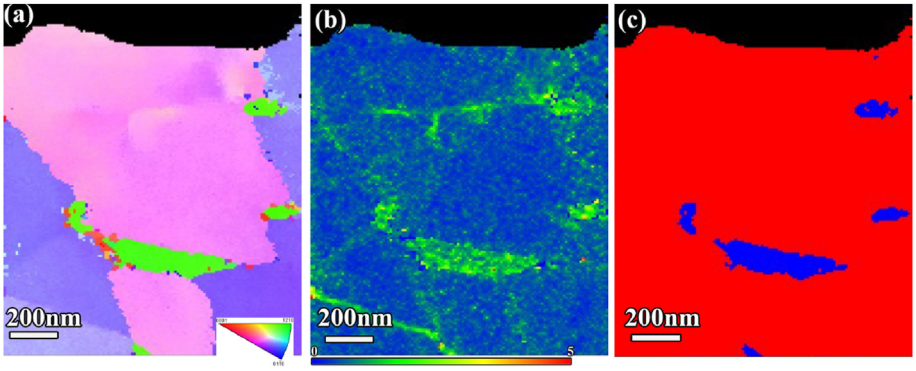

Fig. 15 – TKD results outside the FGA region in Fig. 11; (a) IPF mapping; (b) KAM mapping; (c) Phase mapping (σ_a = 280 MPa, $N_f = 3.510 \times 10^8$).

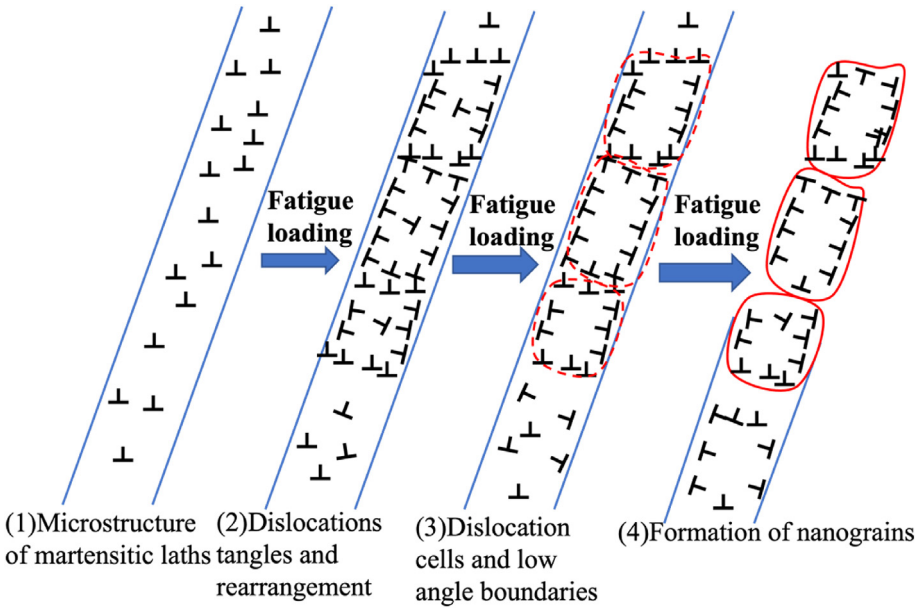

Fig. 16 – Schematic diagram of grain refinement process for martensitic laths.

In the VHCF regime at R = −1, the accumulation of localized massive compression cyclic deformation on the internal crack surface with crack closure effect makes microstructural fragmentation (i.e. martensitic laths fragmentation in the LPBF Ti6Al4V alloy) and grain refinement [9,27,44]. Fig. 16 demonstrates a schematic diagram of the grain refinement process of martensitic laths. Compressive stresses provide the driving force needed for microstructure fragmentation, while a large amount of cyclic loading provides the time needed for grain refinement of martensitic laths. Therefore, with the accumulation of cyclic deformation, the intercrystalline dislocation density increases, and dislocations aggregate, forming the dislocation tangles in the martensitic laths. These high-density dislocation regions become new barriers to dislocation slip, and as cyclic deformation proceeds, the initial grain interior is gradually separated and broken by dislocation tangle regions, developing into some deformed cellular substructures, that is, dislocation cells, which further form the nanograin structures; and dislocations occur in the cell wall rearrangement, which later forms the low angle boundary. This further develops into the FGA region with a nano-grain layer of crack initiation and early propagation in VHCF regime for the LPBF Ti6Al4V alloy.

Fig. 17 represents the interior fatal defect-induced microcrack initiation and initial growth process in the FGA region in VHCF regime at R = −1. In parallel with the formation of nanograins, owing to the strain incompatibility between the defects and the microstructure matrix, microcracks are easily initiated at the interface between the two. As the cyclic loading grows, the microcracks expand at a very low rate in the environment of vacuum inside the specimen, and the low angle boundaries of the nanograins also inhibit the microcrack expansion. At a simultaneous time, microvoids may be formed in the nanograins layer due to plastic deformation subjected to continuous VHCF. However, these microvoids may also originate from the LPBF process, but their sizes are much smaller than the size of the fatal defect. The microvoids generated either before or during fatigue loading will contribute to the merging of microvoids with each other during the subsequent cyclic loading process, which in turn

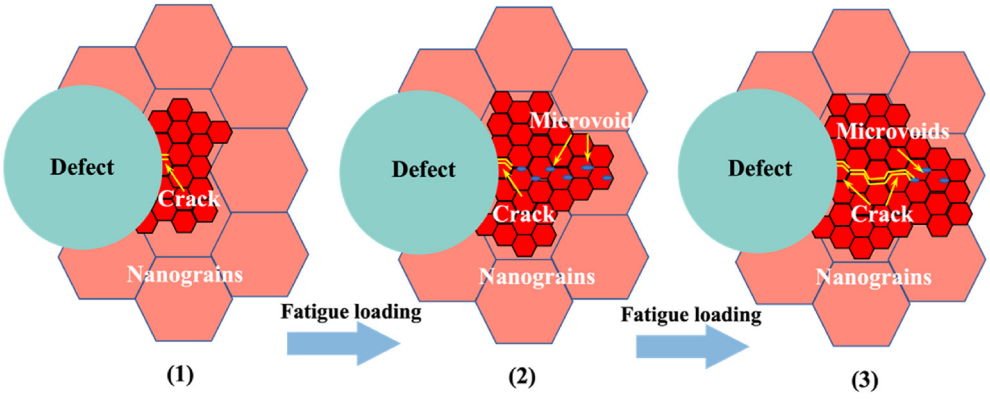

Fig. 17 – The interior defect induced microcrack initiation and initial growth process inside the FGA region in VHCF regime for LPBF Ti6Al4V alloys.

will accelerate the expansion of microcracks. Of course, the microcracks and the merged microvoids connected with each other gradually develop into main cracks and eventually form FGA features.

4. Conclusions

Fatigue behaviors of LPBF fabricating Ti6Al4V alloys subjected to the VHCF regime were investigated. The interior defect induced crack initiation mechanism and initial propagation were analyzed and discussed based on dislocation motions. The main conclusions are as follows:

1. P–S–N curves were obtained by using a three-parameter fitting for LPBF Ti6Al4V alloy at 10% and 90% failure probabilities. And it was verified that the logarithmic form of the fatigue life at each stress amplitude could satisfy the normal distribution.
2. Fatigue cracks were initiated from defects formed during the LPBF manufacturing process. The fracture surface showed typical VHCF characteristics with a smooth and flat fracture in the crack propagation area. A fine granular area (FGA) was formed around the defect and the grain size inside the FGA region was variable.
3. The cracks inside the early stages of FGA formation were driven by the maximum shear stress and growth as mixed Mode II + III cracks, while the cracks outside the FGA were driven by the normal stress and expanded as Mode I cracks.
4. The FGA region is composed of many nanograins and residues of martensitic laths after fragmentation with high dislocation density. Dislocation entanglement and rearrangement form dislocation cells, which further develop into the nanograins and low angle boundaries. Besides, by the action of plastic deformation, the microcrack and microvoids in the FGA layer will merge and aggregate with each other into the main crack and thus accelerate the crack expansion.

Data availability

The data that support the findings of this study are available from the corresponding author upon reasonable request.

Declaration of Competing Interest

The authors declare that they have no known competing financial interests or personal relationships that could have appeared to influence the work reported in this paper.

Acknowledgments

This work was supported by the National Natural Science Foundation of China (No. 12172238, No. 12022208, No. 12102280 and No. 12002226), the National Key Research and Development Program of China (No. 2018YFE0307104), and the Applied Basic Research Programs of Sichuan Province (22YYJC0941 and 22YYJC2301). This work was also funded by China Scholarship Council. In addition, the authors would also like to thank Yang Liu and Chaopeng Zhang for their experimental help.

REFERENCES

[1] Sanaei N, Fatemi A. Defects in additive manufactured metals and their effect on fatigue performance: a state-of-the-art review. Prog Mater Sci 2020;117:100724–65.
[2] Liu S, Shin YC. Additive manufacturing of Ti6Al4V alloy: a review. Mater Des 2019;164(52):107552–62.
[3] Herzog D, Seyda V, Wycisk E, Emmelmann C. Additive manufacturing of metals. Acta Mater 2016;117:371–92.
[4] Kumar P, Prakash O, Ramamurty U. Micro-and meso-structures and their influence on mechanical properties of selectively laser melted Ti-6Al-4V. Acta Mater 2018;154:246–60.
[5] Liu F, He C, Chen Y, Zhang H, Wang Q, Liu Y. Effects of defects on tensile and fatigue behaviors of selective laser melted titanium alloy in very high cycle regime. Int J Fatig 2020;140.
[6] Liu X, Wu Q, Su S, Wang Y. Evaluation and prediction of material fatigue characteristics under impact loads: review and prospects. Int J Struct Integr 2022;13:251–77.
[7] Deng Q-Y, Zhu S-P, He J-C, Li X-K, Carpinteri A. Multiaxial fatigue under variable amplitude loadings: review and solutions. Int J Struct Integr 2022;13:349–93.
[8] Kumar P, Ramamurty U. Microstructural optimization through heat treatment for enhancing the fracture toughness and fatigue crack growth resistance of selective laser melted Ti 6Al 4V alloy. Acta Mater 2019;169:45–59.
[9] Sun C, Chi W, Wang W, Duan Y. Characteristic and mechanism of crack initiation and early growth of an additively manufactured Ti-6Al-4V in very high cycle fatigue regime. Int J Mech Sci 2021;205.
[10] Günther J, Krewerth D, Lippmann T, Leuders S, Tröster T, Weidner A, Biermann H, Niendorf T. Fatigue life of additively manufactured Ti–6Al–4V in the very high cycle fatigue regime. Int J Fatig 2017;94:236–45.
[11] Zhu Y-y, Chen B, Tang H-b, Cheng X, Wang H-m, Li J. Influence of heat treatments on microstructure and mechanical properties of laser additive manufacturing Ti-5Al-2Sn-2Zr-4Mo-4Cr titanium alloy. Trans Nonferrous Metals Soc China 2018;28(1):36–46.
[12] Tan K, Postel V, Liu Y, Yang D, Tang S, Wang C, et al. Development of a photomicroscope method for in situ damage monitoring under ultrasonic fatigue test. Int J Struct Integr 2022;13:237–50.
[13] Wang QY, Bathias C, Kawagoishi N, Chen Q. Effect of inclusion on subsurface crack initiation and gigacycle fatigue strength. Int J Fatig 2002;24(12):1269–74.
[14] Chen Y, He C, Liu F, Wang C, Xie Q, Wang Q, Liu Y. Effect of microstructure inhomogeneity and crack initiation environment on the very high cycle fatigue behavior of a magnesium alloy. Int J Fatig 2020;131.
[15] Du L, Pan X, Qian G, Zheng L, Hong Y. Crack initiation mechanisms under two stress ratios up to very-high-cycle fatigue regime for a selective laser melted Ti-6Al-4V. Int J Fatig 2021;149.
[16] Wang T, Zhu YY, Zhang SQ, Tang HB, Wang HM. Grain morphology evolution behavior of titanium alloy components during laser melting deposition additive manufacturing. J Alloys Compd 2015;632:505–13.

[17] Lin X, Li Y, Wang M, Feng L, Chen J, Huang W. Columnar to equiaxed transition during alloy solidification. Sci China, Ser A: Technol. Sci. 2003;46(5):475–89.
[18] Liu Y, Chen Y, He C, Liu F, Yang K, Li L, Zhang H, Wang C, Wang Q. Vacuum retarding and air accelerating effect on the high-cycle and very-high-cycle fatigue behavior of a ZK60 magnesium alloy. Mater Des 2021;198.
[19] Bathias C, Paris PC. Gigacycle fatigue in mechanical practice. CRC Press; 2004.
[20] Liu F, Chen Y, He C, Li L, Wang C, Li H, Zhang H, Wang Q, Liu Y. Tensile and very high cycle fatigue behaviors of a compressor blade titanium alloy at room and high temperatures. Mater Sci Eng A 2021;811.
[21] Luo Y, Wu S, Zhao X, Hu Y, Li C, Shen Z, Zhong X. Three-dimensional correlation of damage criticality with the defect size and lifetime of externally impacted 25CrMo4 steel. Mater Des 2020;195.
[22] Bantounas I, Dye D, Lindley TC. The role of microtexture on the faceted fracture morphology in Ti–6Al–4V subjected to high-cycle fatigue. Acta Mater 2010;58(11):3908–18.
[23] Oguma H, Nakamura T. The effect of microstructure on very high cycle fatigue properties in Ti–6Al–4V. Scr Mater 2010;63(1):32–4.
[24] Heinz S, Eifler D. Crack initiation mechanisms of Ti6Al4V in the very high cycle fatigue regime. Int J Fatig 2016;93:301–8.
[25] Hong Y, Lei Z, Sun C, Zhao A. Propensities of crack interior initiation and early growth for very-high-cycle fatigue of high strength steels. Int J Fatig 2014;58:144–51.
[26] Liu H, Wang H, Huang Z, Wang Q, Chen Q. Comparative study of very high cycle tensile and torsional fatigue in TC17 titanium alloy. Int J Fatig 2020;139.
[27] Hong Y, Liu X, Lei Z, Sun C. The formation mechanism of characteristic region at crack initiation for very-high-cycle fatigue of high-strength steels. Int J Fatig 2016;89:108–18.
[28] Li W, Xing X, Gao N, Wang P. Subsurface crack nucleation and growth behavior and energy-based life prediction of a titanium alloy in high-cycle and very-high-cycle regimes. Eng Fract Mech 2019;221.
[29] Shiozawa K, Morii Y, Nishino S, Lu L. Subsurface crack initiation and propagation mechanism in high-strength steel in a very high cycle fatigue regime. Int J Fatig 2006;28(11):1521–32.
[30] Grad P, Reuscher B, Brodyanski A, Kopnarski M, Kerscher E. Mechanism of fatigue crack initiation and propagation in the very high cycle fatigue regime of high-strength steels. Scr Mater 2012;67(10):838–41.
[31] Xu L, Wang Q, Zhou M. Micro-crack initiation and propagation in a high strength aluminum alloy during very high cycle fatigue. Mater Sci Eng A Struct Mater Propert Microstruct Process 2018;715:404–13.
[32] Yang K, Chao H, Qi H, Zhi YH, Cong W, Wang Q, Yong JL, Zhong B. Very high cycle fatigue behaviors of a turbine engine blade alloy at various stress ratios. Int J Fatig 2017;99:35–43.
[33] Su H, Liu X, Sun C, Hong Y. Nanograin layer formation at crack initiation region for very-high-cycle fatigue of a Ti-6Al-4V alloy. Fatig Fract Eng Mater Struct 2017;40(6):979–93.
[34] Zhu M, Jin L, Xuan F. Fatigue life and mechanistic modeling of interior micro-defect induced cracking in high cycle and very high cycle regimes. Acta Mater 2018;157:259–75.
[35] Van Swam L, Pelloux R, Grant N. Fatigue behavior of maraging steel 300. Metall Trans A 1975;6(1):45–54.
[36] Koster M, Wagner G, Eifler D. Cyclic deformation behavior of a medium carbon steel in the VHCF regime. Procedia Eng 2010;2(1):2189–97.
[37] Liu F, Chen Y, He C, Liu Y, Wang Q. Very long life fatigue failure mechanism of electron beam welded joint for titanium alloy at elevated temperature. Int J Fatig 2021;152.
[38] Li W, Sun R, Wang P, Li X, Zhang Y, Hu T, Li C, Sakai T. Subsurface faceted cracking behavior of selective laser melting Ni-based superalloy under very high cycle fatigue. Scr Mater 2021;194.
[39] Ke Wang ML, Liu Qing. Evolution mechanisms of the primary α and β phases during α/β deformation of an α/β titanium alloy TC8. Mater Char 2016;120:115–23.
[40] Li L, Li MQ, Luo J. Mechanism in the β phase evolution during hot deformation of Ti–5Al–2Sn–2Zr–4Mo–4Cr with a transformed microstructure. Acta Mater 2015;94:36–45.
[41] Chai G, Forsman T, Gustavsson F, Wang C. Formation of fine grained area in martensitic steel during very high cycle fatigue. Fatig Fract Eng Mater Struct 2015;38(11):1315–23.
[42] Spriestersbach D, Kerscher E. The role of local plasticity during very high cycle fatigue crack initiation in high-strength steels. Int J Fatig 2018;111:93–100.
[43] Pan X, Xu S, Qian G, Nikitin A, Shanyavskiy A, Palin-Luc T, Hong Y. The mechanism of internal fatigue-crack initiation and early growth in a titanium alloy with lamellar and equiaxed microstructure. Mater Sci Eng A 2020;798.
[44] Song Q, Sun C. Mechanism of crack initiation and early growth of high strength steels in very high cycle fatigue regime. Mater Sci Eng A 2020;771.